

Article

Study on Solidification and Stabilization of Antimony-Containing Tailings with Metallurgical Slag-Based Binders

Yunyun Li ^{1,2,3}, Wen Ni ^{1,2,3,*}, Wei Gao ^{2,3,4} , Siqi Zhang ^{1,2,3} , Pingfeng Fu ^{1,2,3}  and Yue Li ^{1,2,3}

¹ School of Civil and Resource Engineering, University of Science and Technology Beijing, Beijing 100083, China; lyyustb@163.com (Y.L.); zsq2017@ustb.edu.cn (S.Z.); pffu@ces.ustb.edu.cn (P.F.); 18532334075@163.com (Y.L.)

² Key Laboratory of Resource-Oriented Treatment of Industrial Pollutants, University of Science and Technology Beijing, Beijing 10083, China; 15201455635@163.com

³ Key Laboratory of High-Efficient Mining and Safety of Metal Mines, Ministry of Education, University of Science and Technology Beijing, Beijing 10083, China

⁴ School of Energy and Environmental Engineering, University of Science and Technology Beijing, Beijing 100083, China

* Correspondence: niwen@ces.ustb.edu.cn

Abstract: Blast furnace slag (BFS), steel slag (SS), and flue gas desulfurized gypsum (FGDG) were used to prepare metallurgical slag-based binder (MSB), which was afterwards mixed with high-antimony-containing mine tailings to form green mining fill samples (MBTs) for Sb solidification/stabilization (S/S). Results showed that all MBT samples met the requirement for mining backfills. In particular, the unconfined compressive strength of MBTs increased with the curing time, exceeding that of ordinary Portland cement (OPC). Moreover, MBTs exhibited the better antimony solidifying properties, and their immobilization efficiency could reach 99%, as compared to that of OPC. $\text{KSb}(\text{OH})_6$ was used to prepare pure MSB paste for solidifying mechanism analysis. Characteristics of metallurgical slag-based binder (MSB) solidified/stabilized antimony (Sb) were investigated via X-ray diffraction (XRD), field emission scanning electron microscopy (SEM), energy dispersive spectroscopy (EDS), Fourier transform infrared spectroscopy (FT-IR), and X-ray photoelectron spectroscopy (XPS). According to the results, the main hydration products of MSB were C-S-H gel and ettringite. Among them, C-S-H gel had an obvious adsorption and physical sealing effect on Sb, and the incorporation of Sb would reduce the degree of C-S-H gel polymerization. Besides, ettringite was found to exert little impact on the solidification and stabilization of Sb. However, due to the complex composition of MSB, it was hard to conclude whether Sb entered the ettringite lattice.

Keywords: metallurgical slag; solidification/stabilization; antimony; steel slag; mine tailings



Citation: Li, Y.; Ni, W.; Gao, W.; Zhang, S.; Fu, P.; Li, Y. Study on Solidification and Stabilization of Antimony-Containing Tailings with Metallurgical Slag-Based Binders. *Materials* **2022**, *15*, 1780. <https://doi.org/10.3390/ma15051780>

Academic Editors: Thomas N. Kerestedjian and Alexander Karamanov

Received: 6 February 2022

Accepted: 23 February 2022

Published: 26 February 2022

Publisher's Note: MDPI stays neutral with regard to jurisdictional claims in published maps and institutional affiliations.



Copyright: © 2022 by the authors. Licensee MDPI, Basel, Switzerland. This article is an open access article distributed under the terms and conditions of the Creative Commons Attribution (CC BY) license (<https://creativecommons.org/licenses/by/4.0/>).

1. Introduction

In 2018, China produced 12.11 billion tons of tailings, accounting for 35.11% of the total production of bulk industrial solid waste. The tailings after mineral processing are usually discarded as solid waste in tailings ponds without any treatment, carrying potential heavy metal pollution risks [1]. Antimony is a toxic metalloid in the group VA of the fifth period of the periodic table. Antimony used in the lead-zinc tailings is mainly stibnite (Sb_2S_3) [2], and many studies reported that the migration and transformation of antimony is mainly $\text{Sb}(\text{OH})_6^-$ [3,4]. In this respect, a series of reactions such as oxidation and leaching occurs under the combined action of oxygen, water, and microorganisms, making Sb_2S_3 soluble SbO_3^- and hydrolyze to $\text{Sb}(\text{OH})_6^-$, and then attached to the surface of various solid particles in the tailings in the form of adsorption [3,5]. This part of antimony usually has high activity, and without proper pretreatment managed, it can cause serious or even catastrophic consequences.

For waste with increased heavy metal concentrations, a feasible management approach may be to landfill the waste [6,7]. At present, the use of cement as a binder for landfill is already a mature technology. Ordinary Portland cement (OPC) is traditionally used for landfill solidification/stabilization (S/S) and has long-term stability [8–11]. For example, there are research reports where Portland cement, fly ash, clay, gypsum, and blast furnace slag were used as solidification/stabilization materials to limit the leaching potential of antimony [12]. According to their results, the leaching rate of antimony-containing waste residue was low and fulfilled the landfill standard, and gypsum was successfully used in immobilizing the antimony. Cornelis investigated the leaching characteristic of antimony by mixing Portland cement with KSb(OH)_6 [13]. They found that various hydration minerals of cement had limited effects on antimony, such as AFm minerals and C-S-H gel. Unfortunately, they did not do a mineralogical analysis to verify the solidifying mechanism of antimony. However, the production of cement is accompanied by the large CO_2 emission, yielding the high cost and limiting the use of the final product [8]. To reduce carbon emissions and to make it possible to absorb a large amount of metallurgical solid waste, blast furnace slag (BFS), steel slag (SS), and flue gas desulfurized gypsum (FGDG) were proposed as cementing binders [14–16]. In the hydration process, BFS provides potentially active silicon–oxygen and aluminum–oxygen tetrahedra, SS is a source of alkaline substances, and FGDG ensures sulfate ions [17,18]. This enables one to form ettringite with low solubility and amorphous C-S-H gels, which enhance the physical and mechanical properties of the cured material to stabilize Sb [13]. At present, most research aimed at evaluating the environmental friendliness of S/S materials and the leaching characteristics of heavy metals using different leaching methods [4,19]. According to our previous research, the metallurgical slag-cementing binders effectively limits the leaching concentration of As and Sb, and the dominant leaching mechanism for Sb is diffusion [14,15,20]. In addition, in our previous research, the solidification mechanism of As was confirmed [21,22]. Arsenic atom can replace the aluminum atom or silicon arsenate with lower solubility, and arsenic can be adsorbed and encapsulated by C-S-H gel [23]. However, as far as we know, there are no relative studies to elucidate the solidifying mechanism of high Sb concentration tailings with metallurgical-slag-based binders from the perspective of mineralogy.

In this study, high-Sb-containing mine tailings (Sb-MT) were immobilized using the total solid waste S/S materials (MSB). The leaching tests were carried out according to HJ 557-2010 Chinese standard to evaluate the immobilization efficiency of antimony and the antimony leaching trend. For better understanding of the immobilization mechanisms of antimony-containing tailings using metallurgical slag-cementing agent, their microscopic characterization was performed via Fourier transform infrared spectroscopy (FT-IR), X-ray photoelectron spectroscopy (XPS), and scanning electron microscopy paired with energy dispersive spectrometer (SEM-EDS).

2. Materials and Experimental Procedures

2.1. Materials

In this study, the materials included BFS, SS, FGDG, high Sb-containing mine tailings (Sb-MT), and ordinary Portland cement PO 42.5 (OPC). Sb-MT samples were purchased from a lead–zinc ore dressing plant in Hechi Nandan, Guangxi province, China. The BFS, SS, and FGDG were provided by Jintaicheng Environmental Resources Co., Ltd., Xingtai, China. The chemical compositions and Blaine fineness values of these materials are given in Table 1. The leaching concentration of antimony in the raw materials was analyzed via inductively coupled plasma atomic emission spectroscopy (ICP-AES). No heavy metals were detected except Sb-MT, with a leaching Sb content of 0.524 mg/L. The XRD pattern of Sb-MT, BFS, SS, and FGDG are shown in Figure 1, revealing the presence of quartz, calcite, and fluorite as the primary phases in the Sb-MT. BFS was mainly in the glassy state, being composed of SiO_2 , CaO, and Al_2O_3 . The primary phases of SS were SiO_2 , CaO, Fe_2O_3 , and

Al_2O_3 , as well as $\beta\text{-C}_2\text{S}$, C_3S , C_3A , and RO phases. The major composition of the FGDG was $\text{CaSO}_4 \cdot 2\text{H}_2\text{O}$.

Table 1. Raw material chemical components, physical properties, concentrations, and leaching concentration of Sb.

Materials		Sb-MT	BFS	SS	FGDG
Chemical composition Oxide (wt. %)	MgO	0.99	8.94	6.00	1.04
	Al_2O_3	4.45	15.43	6.24	0.78
	SiO_2	40.34	24.76	18.16	2.03
	SO_3	17.31	0.83	0.29	44.97
	CaO	15.15	46.16	42.58	45.31
	Fe_2O_3	17.52	2.52	17.66	0.48
Blaine fineness (m^2/Kg)		-	400	400	360
pH		7.35	11.92	12.28	7.85
Leaching Sb concentration ($\mu\text{g}/\text{L}$)		524	ND	ND	ND

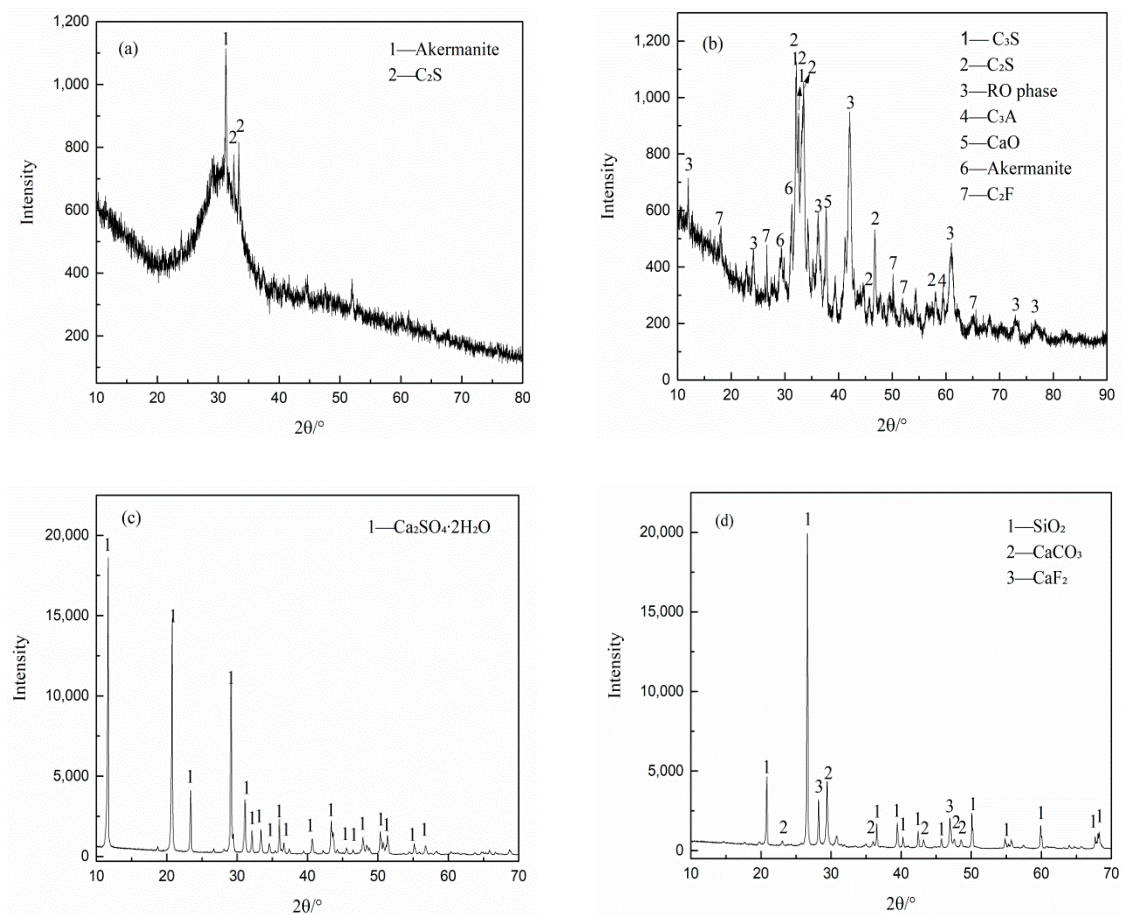


Figure 1. X-ray diffraction (XRD) patterns of raw materials: (a) blast furnace slag (BFS); (b) steel slag (SS); (c) flue gas desulfurized gypsum (FGDG); (d) high Sb-containing mine tailings (Sb-MT).

2.2. Mixture Proportion of Mining Fill Samples

The relative weight percentages of the cementitious materials correspond to those from Ref. [22] and are given in Table 2. OPC was used as cementitious material for the control group treatment. Slump tests were completed according to GB/T 2419-2005 Chinese standard. The slumps of MBT and OPC were both 300 mm, respectively, indicating their good workability.

Table 2. Proportions of total solid waste S/S materials (MSB) components, including equivalent binder-tailings ratio and solid concentration of green mining fill (MBT) samples.

Notation	MSB (Mass Fraction/wt. %)			Binders/Tailings (<i>w/w</i>)	Solid Concentration ^a (wt. %)
	BFS	SS	FGDG		
MBT	60	30	10	$\frac{1}{4}$	86
OPC ^b		100(OPC)			

^a Solid concentration = (binders + tailings)/(binders + tailings + water). ^b OPC used as a cementitious material for the control group.

2.3. Experimental Procedures

The MBT pastes were poured into 50 × 50 × 50 mm³ steel molds, and then cured in a curing chamber (at the relative humidity of approximately 90% and 40 °C, mimicking the conditions of underground mine storage in Guangxi) [22]. The unconfined compressive strength (UCS) of the specimens was assessed as according to GB/T17671-1999 standard at curing times of 3 d, 7 d, 28 d, and 90 d.

Toxicity characteristic leaching tests were conducted via the horizontal vibration method using MBT and OPC at curing times of 3 d, 7 d, 28 d, and 90 d [21].

MSBs were prepared using a 300 mg/L K₂Sb(OH)₆ solution to investigate the hydration and curing mechanisms. All the samples were crushed and terminated with pure ethyl alcohol after 3 d, 7 d, and 28 d, respectively.

X-ray diffraction (XRD) was identified the pastes of the hydration products. XRD analysis was performed on an Ultima IV X-ray diffractometer (Rigaku Mechatronics Co., Ltd, Akishima-shi, Tokyo, Japan) with a copper K α radiation source ($\lambda = 1.5406 \text{ \AA}$) operating at 30 mA and 50 kV. The scan step was 0.02°, and the scan 2 θ was from 5° to 70°.

The microstructure of hydrated pastes was observed via field emission scanning electron microscope (SUPRA 55, Carl Zeiss, Oberkochen, Germany). The working voltage was 10 kV, at a vacuum level lower than 9.9×10^{-6} mbar. The chemical compositions of hydration products were analyzed using an energy dispersive X-ray spectrometer (EDX, Carl Zeiss, Oberkochen, Germany) coupled with FE-SEM.

Structural and chemical bond characterization was performed via Fourier transform infrared spectroscopy (FT-IR). The FT-IR spectra of the samples were recorded in 350–4000 cm⁻¹ using a NICOLET470 infrared spectrometer (ThermoFisher, Maltham, MassachusettsUS), at a sensitivity of 4 cm⁻¹.

The chemical states of the elements were used X-ray photoelectron spectroscopy (XPS). The measurements were done at room temperature under a vacuum of 7×10^{-9} mbar by means of an XPS system (AXIS ULTRA^{DL}, kratos Analytical Ltd., Kyoto, Japan) using a nonmonochromatic Al K α radiation source (1486.6 eV). The scanned surface area was 700 $\mu\text{m} \times 300 \mu\text{m}$. During the XPS experiments, the C1s signal of adventitious hydrocarbons (284.8 eV) serves as the reference line.

3. Results

3.1. UCS Test Results

Figure 2 displays the unconfined compressive strengths of MBT and OPC with increasing curing time. In both cases, the UCS values were above 1 MPa, meaning that the samples satisfied the requirements for mining backfills. Meanwhile, the unconfined compressive strength of MBT was higher than that of OPC, indicating that metallurgical slag-cementing agent had good mechanical performance and broad application prospects.

3.2. Toxicity Characteristic Leaching Test (HJ 557-2010)

Figure 3 depicts the pH levels of the leachate and the leached Sb, as well as the immobilization efficiency of MBT and OPC samples, after 3 d, 7 d, 28 d, and 90 d of curing. In all samples, the leaching of Sb was higher than 5 μL (the Sb limit for the underground class III water according to GB/T 14848-2017 standard). The release of Sb increased with

increasing curing time in the MBT and OPC specimens, and antimony shows high release after 28 days of curing. But the leaching of Sb in MBT sample was lower than that in OPC over the whole curing time range. Even if the leaching of Sb increased with curing time, a huge improvement between 3 d, 7 d, 28 d, and 90 d of immobilization could be seen. Besides, the immobilization efficiency for Sb after three and seven days of curing was up to 99%, and after 90 days, it was more than 90%. Based on the leaching results, it could be confirmed that MBT had the better curing performance of Sb. The higher UCS of MBT was attributed to the formation of more hydration products, which yielded a denser structure and thus reduced the release of Sb from tailings [24].

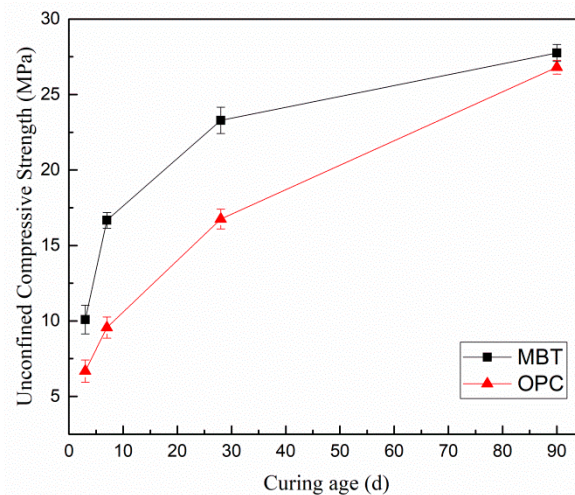


Figure 2. Unconfined compressive strength (UCS) results of MBT and OPC at different curing times.

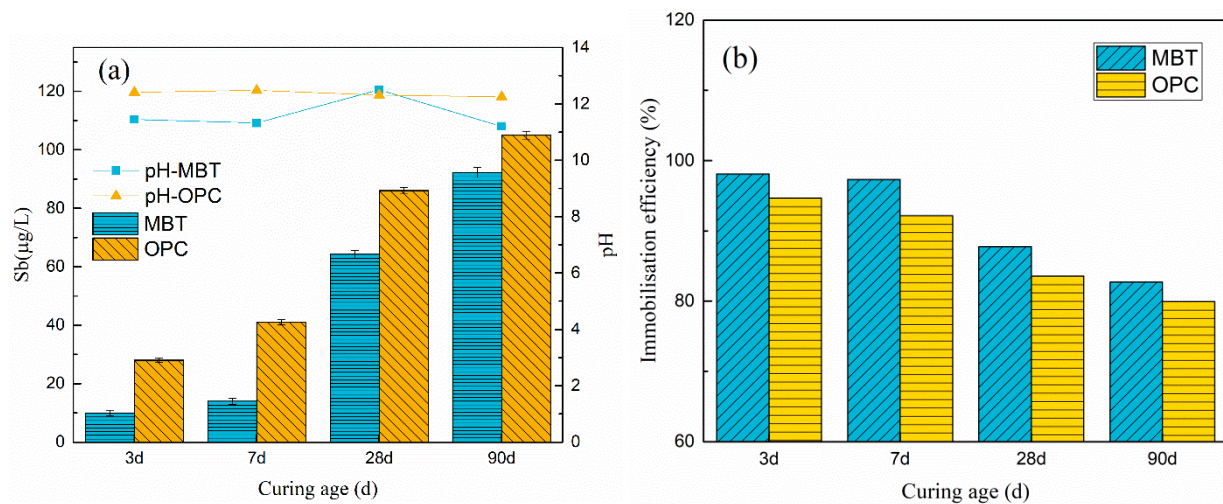


Figure 3. (a) Evolution of pH and Sb release for each MBT and ordinary Portland cement (OPC) sample; (b) immobilization efficiency of Sb after 3 d, 7 d, 28 d, and 90 d of curing during horizontal vibration leaching method.

3.3. Microscopic Analysis

Figure 4 depicts the FE-SEM and EDS results for MBT and OPC after 28 days of aging. In both cases, the main hydration products were ettringite and C-S-H gel [25]. Compared with OPC, MBT exhibited a higher amount of C-S-H gel after 28 days of hydration, while OPC was rich in ettringite. In this respect, the above discussed high compressive strength of MBT (Figure 1) was attributed to the fact that ettringite acted as a skeleton and C-S-H gel served as a filler, making the structure of MBT denser. However, ettringite crystals in OPC were larger than in MBT. As a result, OPC had a less dense structure than MBT.

Moreover, the EDS data (Figure 5) revealed that C-S-H gel was the main host mineral of Sb. Since C-S-H gel has a very high specific surface energy [22], its adsorption and physical encapsulation might be the main reason for why the fixing performance of antimony with MBT was better than that with OPC.

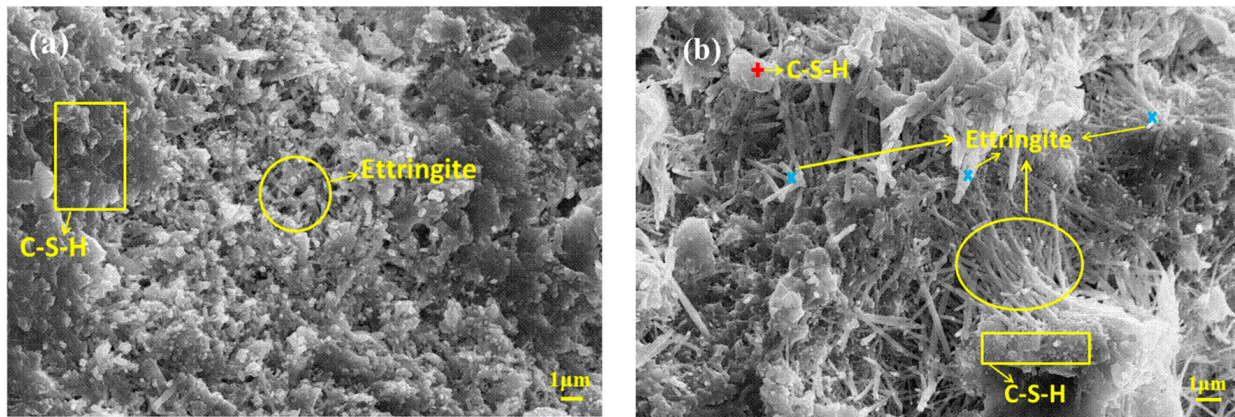


Figure 4. Scanning electron microscope (SEM) images of MBT with OPC at curing age of 28 days: (a) MBT (b) OPC.

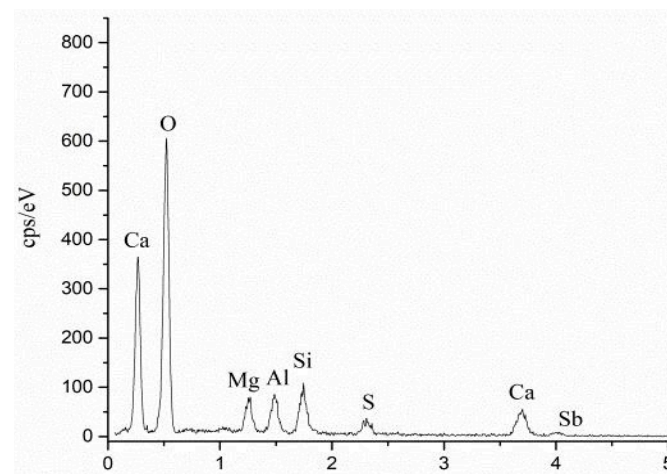


Figure 5. Area of MBT-C-S-H at curing age of 28 days.

3.4. XRD Results

XRD patterns of two pastes after different periods of aging are shown in Figure 6. The main hydration products of pure MSB were ettringite and C-S-H gel, where the peak ($2\theta = 26.6^\circ$) intensity associated with ettringite increased over time. However, the signal from ettringite in MSB-Sb showed an opposite trend, gradually decreasing with aging, just as the peaks at 2θ close to 10° and 26.6° . In addition, the peak positions of ettringite and C-S-H gel were slightly offset in MSB-Sb after 28 days of curing. No antimony phase was found in MSB-Sb. This was because calcium antimony has a highly variable structure, both crystalline and amorphous. In addition, it might also be because of the low content of crystalline calcium antimony falling below the detection limit of XRD, which is generally 1–2 wt. % [26].

3.5. FT-IR Results

Figure 7 displays the FT-IR spectra of MSB-Sb and pure MSB pastes after 3 and 28 days of hydration. In both cases, the spectrograms were rather similar, presenting analogous absorption bands. The wide bands around 3624 cm^{-1} and 3427 cm^{-1} are associated with the vibration of OH-groups in water, whereas the band at 1656 cm^{-1} is a well-defined H-O-

H deformation band from interlayer water [27]. The peak at 1114 cm^{-1} can be attributed to a $[\text{SO}_4]$ stretching mode (ν_3) [28]. In addition, the bands at 611 cm^{-1} and 667 cm^{-1} are related to the symmetric stretching and bending vibration of Al-OH species in the $[\text{Al}(\text{OH})_6]^{3-}$ substructure of ettringite. The feature at 977 cm^{-1} is the antisymmetric Si-O(Al) stretching vibration which is characteristic of C-S-H gel. The bands at 513 cm^{-1} and 451 cm^{-1} are caused by the out-of-plane banding vibration and in-plane bending vibration of Si-O, respectively [14,29–31]. The only difference between MSB-Sb and MSB was that the absorption peaks related to C-S-H gel in MSB-Sb shifted to the wavelet numbers. This indicated that the incorporation of Sb into the cementing material had a significant effect on the hydration product C-S-H gel, which was manifested by a decrease in the degree of polymerization of C-S-H [17].

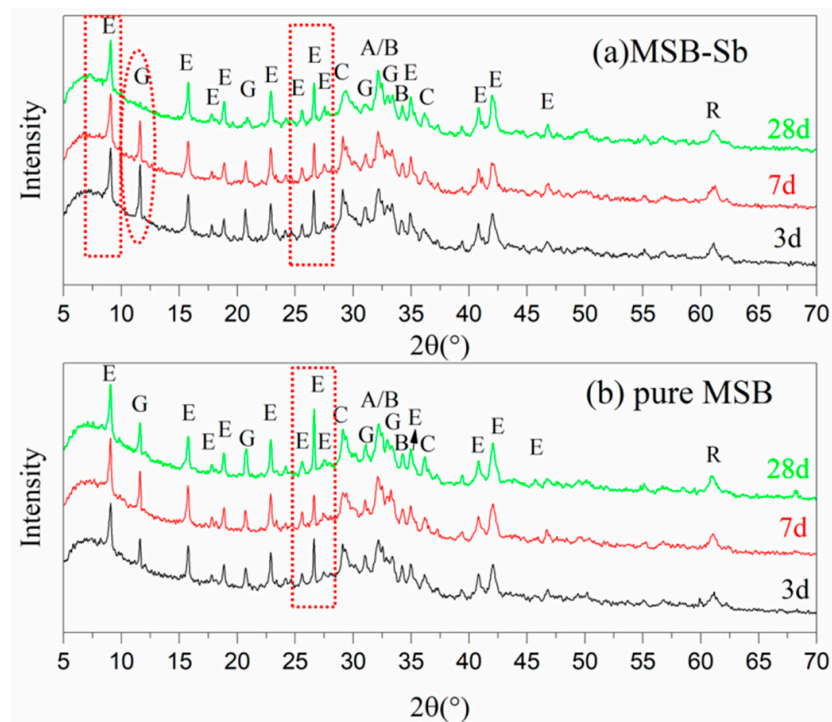


Figure 6. XRD patterns of pastes after 3 d, 7 d, and 28 d of aging. (a) MSB-Sb; (b) pure MSB. Here, phase designations are as follows: A: Alite (Ca_3SiO_5 , C_3S); B: Belite (Ca_2SiO_2 , C_2S); C: C-S-H gel; E: Ettringite ($\text{Ca}_6\text{Al}_2(\text{SO}_4)_3(\text{OH})_{12}\cdot 26\text{H}_2\text{O}$); G: Gypsum ($\text{CaSO}_4\cdot 2\text{H}_2\text{O}$); R: RO phase.

3.6. XPS Spectra

Table 3 displays the binding energies of main elements in the Sb cured sample and the blank group after 28 days of curing. As seen from the table, the binding energies of Ca, O, and Si atoms in the Sb cured sample slightly decreased with respect to those the reference groups, indicating that the incorporation of Sb exerted a great influence on silicate. Moreover, the covalent radius of Sb atom (1.39 \AA) is larger than those of Al (1.21 \AA) and Si (1.11 \AA), making it difficult for Sb to undergo homogeneity substitution with Al and Si in C-S(A)-H gel [32]. In addition, Sb has a high electronegativity (1.9) [19]. If Sb enters the silicon (aluminum) oxygen tetrahedron, it will inevitably lead to a decrease in the outer electron cloud density of other surrounding ions and an increase in the binding energy of atoms [33]. However, according to Table 3, the binding energy of Al remained unchanged, while that of Si decreased during aging. Combined with the above SEM and IR results (Figures 4 and 7), one may conclude that Sb was mainly adsorbed and wrapped in C-S(A)-H gel.

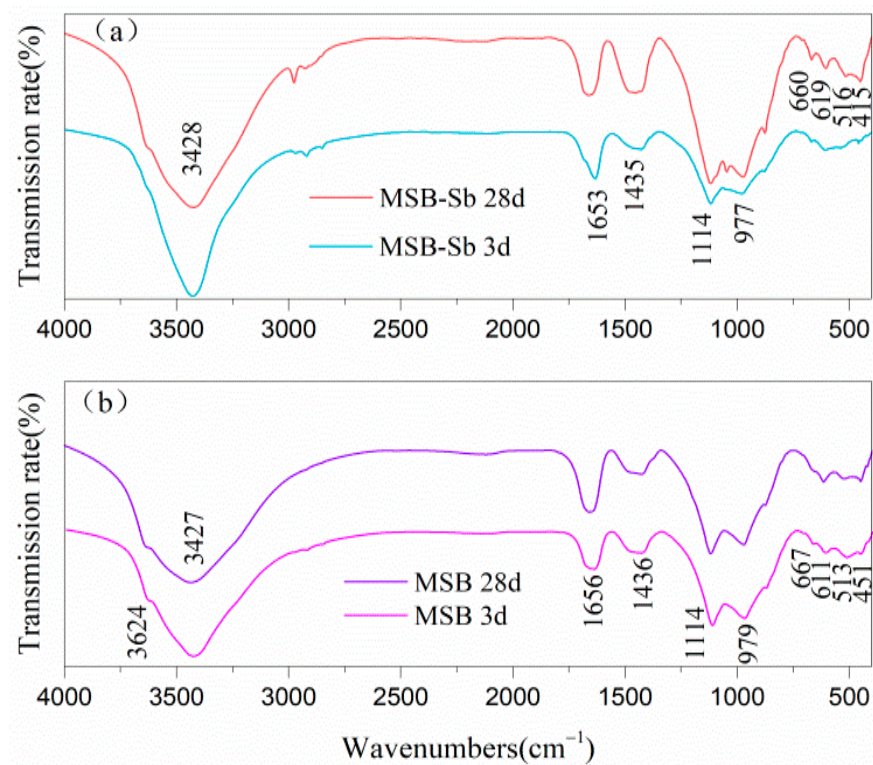


Figure 7. FT-IR spectra of pastes after 3 and 28 days of curing: (a) MSB with Sb; (b) pure MSB.

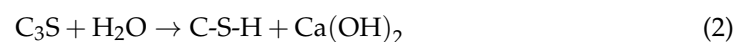
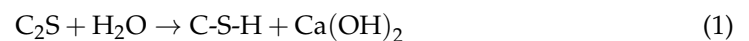
Table 3. Changes in binding energies of main elements in Sb cured sample and blank group after 28 days of curing.

Elements	Ca	Al	Si	O	S
Blank group	347.30	74.26	102.10	531.67	168.99
Sb cured sample	347.11	74.26	102.00	531.54	169.21
Changes	−0.19	0	−0.10	−0.13	+0.22

4. Discussions

Among the cementitious materials, the BFS with vitreous structure has strong chemical activity. The vitreous body of the slag is mainly composed of silicon–oxygen tetrahedrons, and some Al^{3+} replaces Si^{4+} to form aluminosilicate tetrahedrons with higher activity than silicon–oxygen tetrahedra, and a small amount of aluminosilicate crystallites with extremely low crystallinity [34].

Figure 8 displays the hydration reaction of MSB and it can be described as follows:



In the early stage of hydration, the amorphous vitreous structure in the blast furnace slag dissociates and dissolves silicate, aluminate, and Ca^{2+} , Al^{3+} , Mg^{2+} ions, and reacts to form C-S(A)-H gel, such as (1) and (2). With the hydration and dissolution of the steel slag, the hydroxyl groups provide a strong alkaline environment for the system. The gel formed on the surface of the slag gradually separates, which makes the polymerization degree of the glass surface of the slag drop rapidly, and thus the remaining glass activity is reactivated, promoting the continuous hydration reaction of the slag. While the slag hydration

continuously consumes hydroxyl groups, the hydration of the steel slag is further promoted. Desulfurized gypsum provides a large amount of Ca^{2+} and SO_4^{2-} ions for the system and enters the reactions with the gel to form ettringite (such as (3)), and the consumption of the gel promotes the hydration of the above-mentioned slag and steel slag [35]. The coordinated excitation of blast furnace slag, steel slag, and desulfurized gypsum is conducive to the mass production of ettringite and C-S-H gel. The C-S-H gel accumulates and encapsulates the ettringite minerals to form a tight and stable structure [28]. Moreover, the large specific surface area of C-S-H gel has great potential to adsorb heavy metals. Although the surface is negatively charged, due to the charge balance, the surface charge is reversed after the adsorption of calcium ions, allowing antimony anions to be adsorbed [36–39]. In addition, antimony precipitates can be tightly encapsulated and sealed by C-S-H gel. $\text{Ca}[\text{Sb}(\text{OH})_6]_2$ precipitates tend to be in equilibrium at the lower pH, while precipitates at higher pH scales are more likely to be romeites ($\text{Ca}_{1+x}\text{Sb}_2\text{O}_6\text{OH}_{2-2x}$) [40], such as (4) [13]. It is different from the incorporation in the ettringite for $\text{Sb}(\text{OH})_6^-$, which has a large octahedral structure. Therefore, the valid immobilization mechanism for $\text{Sb}(\text{OH})_6^-$ is to be adsorbed on the ettringite surface rather than incorporated into the structure [31,40]. In this study, the adsorption of Sb by ettringite was not proved and needs to be further verified in the synthesis of single mineral ettringite.

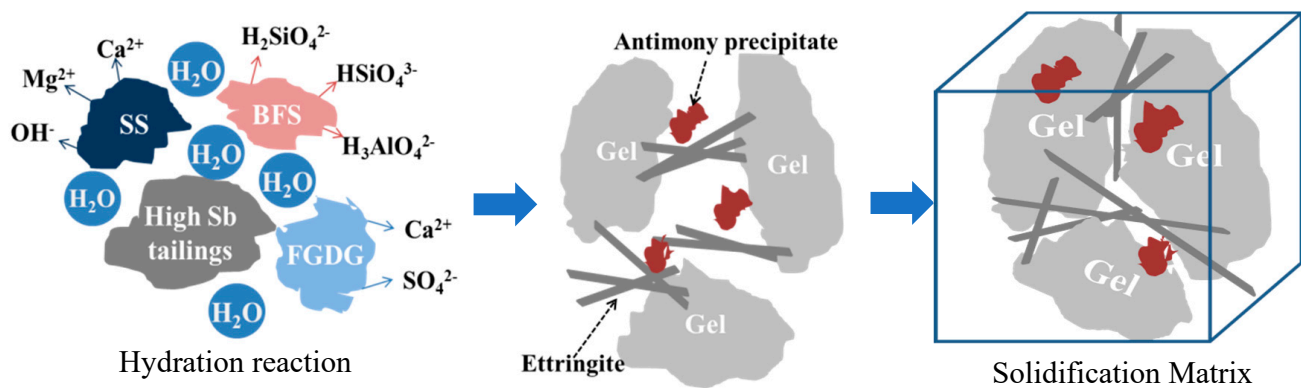


Figure 8. Schematic diagram of curing mechanism of Sb in metallurgical-slag-based materials.

According to the current knowledge, in Hebei and Guangxi provinces, the purchase price of raw materials SS, BFS, and FG DG is about 10 yuan/t, 120 yuan/t, and 15 yuan/t respectively, while SS is no charged in many areas. The original price of MSB material is $10 \times 0.3 + 120 \times 0.6 + 15 \times 0.1 = 76.5$ yuan/t, plus 130 yuan of processing fee and 20% profit of enterprises, and the price of MSB is 247.8 yuan. This is much lower than 450 yuan/t of cement. In addition, it also avoids CO_2 emissions from calcination of limestone during cement production.

5. Conclusions

The solidified bodies of metallurgical slag and ordinary Portland cement (OPC)-solidified antimony were compared via compressive strength measurements and horizontal oscillation method, and pure slurry was prepared to elucidate the mineralogical solidification mechanism of metallurgical slag to antimony. The following conclusions were drawn:

1. Green mining fill samples (MBT) exhibited higher strength and a more pronounced antimony fixation effect than those of OPC.
2. No newly formed antimony-containing mineral phase was detected in the metallurgical slag, but it was mainly surrounded by the adsorbed gel.
3. Even though the heavy metal antimony was found to be able to reduce the degree of polymerization in the gel, its influence on ettringite and its relationship are not yet proven.

Author Contributions: Conceptualization, W.N. and Y.L. (Yunyun Li); methodology, W.G., Y.L. (Yunyun Li); validation, Y.L. (Yunyun Li), W.N., and S.Z.; formal analysis, Y.L. (Yunyun Li); investigation, Y.L. (Yue Li); resources, W.N., P.F.; data curation, Y.L. (Yunyun Li); writing—original draft preparation, Y.L. (Yunyun Li), S.Z., and Y.L. (Yue Li); writing—review and editing, Y.L. (Yunyun Li); visualization, W.G., Y.L. (Yue Li); supervision, W.N.; project administration, W.N., P.F.; funding acquisition, P.F. All authors have read and agreed to the published version of the manuscript.

Funding: This work was funded by National Key Research and Development Program of China, grant number 2020YFC1807804.

Institutional Review Board Statement: Not applicable.

Informed Consent Statement: Not applicable.

Data Availability Statement: Not applicable.

Acknowledgments: Thanks to Xiaoyan Huang for revising the language of the manuscript.

Conflicts of Interest: The authors declare no conflict of interest.

References

1. Nishad, P.A.; Bhaskarapillai, N. Antimony, a pollutant of emerging concern: A review on industrial sources and remediation technologies. *Chemosphere* **2021**, *277*, 130252. [[CrossRef](#)]
2. Ashley, P.M.; Craw, D.; Graham, B.P.; Chappell, D.A. Environmental mobility of antimony around mesothermal stibnite deposits, New South Wales, Australia and southern New Zealand. *J. Geochem. Explor.* **2003**, *77*, 1–14. [[CrossRef](#)]
3. Zhang, Y.; Ding, C.X.; Gong, D.X.; Deng, Y.C.; Huang, Y.; Zheng, J.F.; Xiong, S.; Tang, R.D.; Wang, Y.C.; Su, L. A review of the environmental chemical behavior, detection and treatment of antimony. *Environ. Technol. Innov.* **2021**, *24*, 102026. [[CrossRef](#)]
4. Corneils, G.; Gerven, T.V.; Vandecasteele, C. Antimony leaching from MSWI bottom ash: Modelling of the effect of pH and carbonation. *Waste Manag.* **2012**, *32*, 278–286. [[CrossRef](#)]
5. Guo, J.L.; Yin, Z.P.; Zhong, W.; Jing, C.Y. Immobilization and transformation of co-existing arsenic and antimony in highly contaminated sediment by nano zero-valent iron. *J. Environ. Sci.* **2022**, *112*, 152–160. [[CrossRef](#)]
6. Xiao, B.L.; Wen, Z.J.; Miao, S.J. Utilization of steel slag for cemented tailings backfill: Hydration, strength, pore structure, and cost analysis. *Case Stud. Constr. Mater.* **2021**, *15*, e00621. [[CrossRef](#)]
7. Almas, A.R.; Pironin, E.; Okkenhaug, G. The partitioning of Sb in contaminated soils after being immobilization by Fe-based amendments is more dynamic compared to Pb. *Appl. Geochem.* **2019**, *108*, 104378. [[CrossRef](#)]
8. Andrew, R.M. Global CO₂ Emissions from Cement Production. *Earth Syst. Sci. Data Discuss.* **2018**, *10*, 195–217. [[CrossRef](#)]
9. Zhang, C.Y.; Han, R.; Yu, B.Y.; Wei, Y.M. Accounting process-related CO₂ emissions from global cement production under Shared Socioeconomic Pathways. *J. Clean. Prod.* **2018**, *184*, 451–465. [[CrossRef](#)]
10. Li, J.S.; Chen, L.; Zhan, B.J.; Wang, L.; Poon, C.S.; Tsang, D.C.W. Sustainable stabilization/solidification of arsenic-containing soil by blast slag and cement blends. *Chemosphere* **2021**, *271*, 129868. [[CrossRef](#)]
11. Wang, L.; Chen, L.; Cho, D.W.; Tsang, D.C.W.; Yang, J.; Hou, D.Y.; Baek, K.; Kua, H.W.; Poon, C.S. Novel synergy of Si-rich minerals and reactive MgO for stabilisation/solidification of contaminated sediment. *J. Hazard. Mater.* **2019**, *365*, 695–706. [[CrossRef](#)]
12. Salihoglu, G. Immobilization of antimony waste slag by applying geopolymerization and stabilization/solidification technologies. *J. Air Waste Manag. Assoc.* **2014**, *64*, 1288–1298. [[CrossRef](#)] [[PubMed](#)]
13. Cornelis, G.; Etschmann, B.; Gerven, T.V.; Vandecasteele, C. Mechanisms and modelling of antimonate leaching in hydrated cement paste suspensions. *Cem. Concr. Res.* **2012**, *42*, 1307–1316. [[CrossRef](#)]
14. Gao, W.; Li, Z.F.; Zhang, S.Q.; Zhang, Y.Y.; Fu, P.F.; Yang, H.F.; Ni, W. Enhancing Arsenic Solidification/Stabilisation Efficiency of Metallurgical Slag-Based Green Mining Fill and Its Structure Analysis. *Metals* **2021**, *11*, 1389. [[CrossRef](#)]
15. Gao, W.; Li, Z.F.; Zhang, S.Q.; Zhang, Y.Y.; Teng, G.X.; Li, X.Q.; Ni, W. Solidification/Stabilization of Arsenic-Containing Tailings by Steel Slag-Based Binders with High Efficiency and Low Carbon Footprint. *Materials* **2021**, *14*, 5864. [[CrossRef](#)] [[PubMed](#)]
16. Rasaki, S.A.; Zhang, B.X.; Guarecuco, R.; Thomas, T.J.; Yang, M.H. Geopolymer for use in heavy metals adsorption, and advanced oxidative processes: A critical review. *J. Clean. Prod.* **2019**, *213*, 42–58. [[CrossRef](#)]
17. Li, J.; Zhang, S.Q.; Wang, Q.; Ni, W.; Li, K.Q.; Fu, P.F.; Hu, W.T.; Li, Z.F. Feasibility of using fly ash–slag-based binder for mine backfilling and its associated leaching risks. *J. Hazard. Mater.* **2020**, *400*, 123191. [[CrossRef](#)]
18. Li, Y.Y.; Ni, W.; Gao, W.; Zhang, Y.Y.; Yan, Q.H.; Zhang, S.Q. Corrosion evaluation of steel slag based on a leaching solution test. *Energy Sources Part A Recovery Util. Environ. Eff.* **2019**, *41*, 790–801. [[CrossRef](#)]
19. Cornelis, G.; Johnson, C.A.; Gerven, T.V.; Vandecasteele, C. Leaching mechanisms of oxyanionic metalloid and metal species in alkaline solid wastes. *Appl. Geochem.* **2008**, *23*, 955–976. [[CrossRef](#)]
20. Gao, W.; Ni, W.; Zhang, Y.Y.; Li, Y.Y.; Shi, T.Y.; Li, Z.F. Investigation into the semi-dynamic leaching characteristics of arsenic and antimony from solidified/stabilized tailings using metallurgical slag-based binders. *J. Hazard. Mater.* **2020**, *381*, 120992. [[CrossRef](#)]

21. Zhang, Y.Y.; Zhang, S.Q.; Ni, W.; Yan, Q.H.; Gao, W.; Li, Y.Y. Immobilisation of high-arsenic-containing tailings by using metallurgical slag-cementing materials. *Chemosphere* **2019**, *223*, 117–123. [[CrossRef](#)] [[PubMed](#)]
22. Zhang, Y.Y.; Gao, W.; Ni, W.; Zhang, S.Q.; Li, Y.Y.; Wang, K.; Huang, X.H.; Fu, P.F.; Hu, W.T. Influence of calcium hydroxide addition on arsenic leaching and solidification/stabilisation behaviour of metallurgical-slag-based green mining fill. *J. Hazard. Mater.* **2020**, *390*, 122161. [[CrossRef](#)]
23. Yan, Q.H.; Ni, W.; Gao, W.; Li, Y.Y.; Zhang, Y.Y. Mechanism for solidification of arsenic with blast furnace slag-steel slag based cementitious materials. *J. Cent. South Univ. (Sci. Technol.)* **2019**, *50*, 1544–1550. [[CrossRef](#)]
24. Li, Y.C.; Wu, J.X.; Hu, W.; Ren, B.Z.; Hursthouse, A.S. A mechanistic analysis of the influence of iron-oxidizing bacteria on antimony (V) removal from water by microscale zero-valent iron. *J. Chem. Technol. Biotechnol.* **2018**, *93*, 2527–2534. [[CrossRef](#)]
25. Yi, H.; Xu, G.P.; Cheng, H.G.; Wang, J.S.; Wan, Y.F.; Chen, H. An Overview of Utilization of Steel Slag. *Procedia Environ. Sci.* **2012**, *16*, 791–801. [[CrossRef](#)]
26. Li, Y.; Qiao, C.y.; Ni, W. Green concrete with ground granulated blast-furnace slag activated by desulfurization gypsum and electric arc furnace reducing slag. *J. Clean. Prod.* **2020**, *269*, 122212. [[CrossRef](#)]
27. Liu, Y.; Ni, W.; Huang, X.Y.; Ma, X.M.; Li, D.Z. Characteristics of hydration and hardening of red mud of bayer process in carbide slag-flue gas desulfurization gypsum system. *Mater. Rep.* **2016**, *30*, 120–124. [[CrossRef](#)]
28. Ni, W.; Li, Y.; Xu, D.; Xu, C.W.; Jiang, Y.Q.; Gao, G.J. Hydration mechanism of blast furnace slag-reduction slag based solid waste cementing materials. *J. Cent. South Univ. (Sci. Technol.)* **2019**, *50*, 2342–2351. [[CrossRef](#)]
29. Eskander, S.B.; Bayoumi, T.A.; Tawfik, M.E. Immobilization of Borate Waste Simulate in Cement-Water Extended Polyester Composite Based on Poly(Ethylene Terephthalate) Waste. *Polym.-Plast. Technol. Eng.* **2006**, *45*, 939–945. [[CrossRef](#)]
30. Zhao, Y.L.; Wu, P.Q.; Qiu, J.P.; Guo, Z.B.; Tian, Y.S.; Sun, X.G.; Gu, X.W. Recycling hazardous steel slag after thermal treatment to produce a binder for cemented paste backfill. *Powder Technol.* **2022**, *395*, 652–662. [[CrossRef](#)]
31. Ines, G.L.; Fernandez-Jimenez, A.; Blanco, M.T.; Palomo, A. FTIR study of the sol-gel synthesis of cementitious gels: C–S–H and N–A–S–H. *J. Sol-Gel Sci. Technol.* **2008**, *45*, 63–72. [[CrossRef](#)]
32. Noam, A. Covalent radii from ionization energies of isoelectronic series. *Chem. Phys. Lett.* **2014**, *595–596*, 214–219. [[CrossRef](#)]
33. Santamaria, L.; Vicente, M.A.; Korili, S.A.; Gil, A. Effect of the preparation method and metal content on the synthesis of metal modified titanium oxide used for the removal of salicylic acid under UV light. *Environ. Technol.* **2018**, *41*, 2073–2084. [[CrossRef](#)]
34. Li, Y.; Wu, B.H.; Ni, W.; Li, X.M. Synergies in Early Hydration Reaction of Slag-Steel Slag-Gypsum System. *J. Northeast. Univ. (Nat. Sci.)* **2020**, *41*, 581–586. [[CrossRef](#)]
35. Avalos, N.M.; Varga, T.; Mergelsberg, S.T.; Silverstein, J.A.; Saslow, A.A. Behavior of iodate substituted ettringite during aqueous leaching. *Appl. Geochem.* **2021**, *125*, 104863. [[CrossRef](#)]
36. Pointeau, I.; Reiller, P.; Mace, N.; Landesman, C.; Coreau, N. Measurement and modeling of the surface potential evolution of hydrated cement pastes as a function of degradation. *J. Colloid Interface Sci.* **2006**, *300*, 33–44. [[CrossRef](#)] [[PubMed](#)]
37. Zou, C.; Long, G.C.; Zheng, X.H.; Ma, C.; Xie, Y.J.; Sun, Z.P. Water evolution and hydration kinetics of cement paste under steam-curing condition based on low-field NMR method. *Constr. Build. Mater.* **2020**, *271*, 121583. [[CrossRef](#)]
38. Elakneswaran, Y.; Nawa, T.; Kurumisawa, K. Electrokinetic potential of hydrated cement in relation to adsorption of chlorides. *Cem. Concr. Res.* **2009**, *39*, 340–344. [[CrossRef](#)]
39. Ochs, M.; Pointeau, I.; Giffaut, E. Caesium sorption by hydrated cement as a function of degradation state: Experiments and modelling. *Waste Manag.* **2006**, *26*, 725–732. [[CrossRef](#)] [[PubMed](#)]
40. Cornelis, G.; Gerven, T.V.; Snellings, R.; Verbinnen, B.; Elsen, J.; Vandecasteele, C. Stability of pyrochlores in alkaline matrices Solubility of calcium antimonate. *Appl. Geochem.* **2011**, *26*, 809–817. [[CrossRef](#)]